# Temperature-Driven Chemical Segregation in Co-Free Li-Rich-Layered Oxides and Its Influence on Electrochemical Performance

Peer-reviewed author version

Rajappa Prakasha, Kunkanadu; Grins, Jekabs; Jaworski, Aleksander; Thersleff, Thomas; Svensson, Gunnar; Josang, Leif Olav; Dyrli, Anne Dalager; PAULUS, Andreas; DE SLOOVERE, Dries; D'HAEN, Jan; VAN BAEL, Marlies; HARDY, An; Avireddy, Hemesh; Ramon Morante, Joan & Jacas Biendicho, Jordi (2022)
Temperature-Driven Chemical Segregation in Co-Free Li-Rich-Layered Oxides and Its Influence on Electrochemical Performance. In: CHEMISTRY OF MATERIALS, 34 (8) , p. 3637 -3647.

DOI: 10.1021/acs.chemmater.1c04150
Handle: http://hdl.handle.net/1942/37518

# Temperature-driven chemical segregation in Co-free Li-rich layered oxides and its influence on electrochemical performance

Kunkanadu Rajappa Prakasha[1*], Jekabs Grins[2], Aleksander Jaworski[2], Thomas Thersleff[2], Gunnar Svensson[2], Leif Olav Jøsang[3], Anne Dalager Dyrli[3], Andreas Paulus[4], Dries De Sloovere[4], Jan D'Haen[4], Marlies K. Van Bael[4], An Hardy[4], Hemesh Avireddy [1], Joan Ramon Morante[1], Jordi Jacas Biendicho[1].

[1]Catalonia Institute for Energy Research-IREC, Sant Adrià de Besòs, 08930 Barcelona, Spain.

[2]Department of Materials and Environmental Chemistry, Stockholm University 106 91 Stockholm, Sweden.

[3]Ceramic Powder Technology AS, Kvenildmyra 6, 7093 Tiller, Norway.

[4]UHasselt, Institute for Materials Research (IMO-Imomec), Imec, division Imomec, and EnergyVille, Agoralaan, Building D, 3590 Diepenbeek, Belgium.

Corresponding author:

Kunkanadu Rajappa Prakasha pkunkanadu@irec.cat

**Abstract**

Co-free Li-rich layered oxides are gaining interest as feasible positive electrode materials in lithium-ion batteries (LIBs) in terms of energy density, cost reduction, and alleviating safety concerns. Unfortunately, their commercialization is hindered by the severe structural degradation that occurs during electrochemical operation. The study at hand demonstrates advanced structural engineering of a Li-rich Co-free oxide with composition $Li_{1.1}Ni_{0.35}Mn_{0.55}O_2$ by spray-pyrolysis and subsequent calcination of an aqueous precursor, creating a segregated structure of two distinct layered phases with space groups $R\bar{3}m$ (rhombohedral) and $C2/m$ (monoclinic) . This particular structure was investigated with powder neutron diffraction, high-resolution analytical transmission electron microscopy imaging, and electron energy loss spectroscopic characterization. This complex structure contributes to the high electrochemical stability and good rate capability observed for this compound (160 mAh/g at C/3 and 100 mAh/g at 1C). These results provide new insights into the feasibility of developing and commercializing of cobalt-free positive electrode materials for LIBs.

**Introduction**

Advanced rechargeable lithium-ion batteries (LIBs) are promising energy storage devices for electric vehicles (EVs) because they can combine a high energy density with an excellent electrochemical stability [1]. An underlying challenge in the development of LIBs is ensuring thermal safety combined with a cost reduction without compromising the high energy density. Currently, LIB technology for consumer EVs is dominated by cobalt-containing $LiNi_xMn_yCo_zO_2$ (NMC) chemistry on the side of the positive electrode. The large-scale production of LIBs containing these materials implies a large reliance on cobalt, which is problematic due to its high cost, scarcity and vulnerable global supply chain. In recent years, there has been a growing consensus between academia and industry to eliminate cobalt in high energy-density cathode materials [2,3].

The development of high performance materials with lower cobalt content (e.g., $LiNi_{0.6}Mn_{0.2}Co_{0.2}O_2$ (NMC622), $LiNi_{0.8}Mn_{0.1}Co_{0.1}O_2$ (NMC811), $LiNi_{1-x-y}Co_xAl_yO_2$ (NCA) has effectively lowered the utilization of cobalt to a certain extent. The parallel increase in nickel content has increased the specific capacity of these materials, at the cost of cycle life, thermal stability, and safety [4]. Additionally, these materials typically suffer from increased moisture sensitivity, $Li^+/Ni^{2+}$ cation mixing and parasitic reactions with the electrolyte at elevated temperatures and above specific potentials. These effects place severe limitations

on cells performance, and put pressure on the LIB technology transition towards ensuring EV safety and sustainability.

Li-rich layered oxides, also termed as composite oxides with general formula [$xLiMO_2*(1-x)Li_2MnO_3$ (M = Mn, Co, Ni, etc.)], are potential alternatives for the compositions described above [5,6]. In these phases, the monoclinic $Li_2MnO_3$ structure closely resembles the rhombohedral $LiMO_2$ structure, composed of alternating lithium- and transition metal layers. These structures differ in cation ordering. The octahedral coordinated $Li^+$ and $Mn^{4+}$ cations in the $Li_2MnO_3$ structure, with formula [$Li(Li_{1/3}Mn_{2/3})O_2$], occupy the transition metal layers in a honeycomb-like order whereas for the $LiMO_2$ structure, the transition metal layers are essentially only occupied by transition metal ions. Li-rich layered oxides may offer a considerably higher practical energy density, owing to the cumulative capacity of anionic and cationic redox processes [7], in addition to a better thermal stability and improved cost-effectiveness because of the high percentage of manganese in the chemical composition [8–10]. Although Li-rich layered oxides meet many requirements for next-generation LIB positive electrode materials, there are several fundamental issues that impede their practical adaption and commercialization. The main issue is the occurrence of severe voltage fade (i.e. decrease of the specific energy) upon galvanostatic cycling, arising from the gradual conversion from the initial layered structure to a spinel-type structure and eventually a rock-salt-type structure. This irreversible structural degradation originates from oxygen loss, combined with reduction of Mn, disproportionation and migration to the lithium layer [11,12]. As this structural degradation starts at the particle's surface, a number of approaches has been introduced to improve the structural and chemical stability by surface engineering (surface coating, surface grafting, anion/cation doping and concentration gradient etc.)[13–16]. Unfortunately, these strategies offered limited extents of improvement. Therefore, novel strategies remain required to achieve a desirable electrochemical performance.

There are several temperature-controlled synthesis studies of Li- and Mn-rich layered oxides in the literature but, to the best of our knowledge, the majority of the available reports focus on relationships between synthesis conditions and particle size and morphology, cation mixing, phase purity, etc.. and their influences on electrochemical performances[17–20]. But the comprehensive studies on the structure evolution of these materials have yet to be fully explored.

This paper presents a simple and effective strategy to improve the electrochemical performance of cobalt-free $Li_{1.1}Ni_{0.35}Mn_{0.55}O_2$ layered oxides. The study explores the impact of calcination on the structure evolution and electrochemical performance of cobalt-free $Li_{1.1}Mn_{0.55}Ni_{0.35}O_2$ oxides. The increase in

calcination temperature leads to an increase in particle size, and to pronounced structural segregation in the particles. These factors mitigate capacity degradation, thereby enhancing the cycle life and rate capability of the cobalt-free positive electrode materials.

**Experimental section**

Co-free Li-rich layered oxides were synthesized by spray pyrolysis. An aqueous solution was prepared by dissolving a stoichiometric amount (Li:Ni:Mn = 1.1:0.35:0.55) of metal nitrates in distilled water mixing individual precursor solutions under stirring. The homogeneous solution was atomized by a two-phase nozzle (pressurized air + solution) into a pre-heated rotating (~2rpm) furnace (Entech Energiteknik AB) under constant air flow, yielding an approximate average residence time of ~2 seconds at 900 °C. This caused instant water vaporization, and onset of nitrate decomposition, as mixed metal oxide began to form. The collected powders were calcined using a Nabertherm NW300 chamber furnace at 700, 800 or 900 °C for 6 h in air with a heating and cooling rates of 200 °C per hour. The synthesized powders were collected after cooling to room temperature. Samples are referred as LNM7 (treated at 700 °C), LNM8 (800 °C) and LNM9 (900 °C) in this manuscript.

Powder X-ray diffraction (PXRD) was performed on a Bruker D2 phaser table-top diffractometer (CuKα radiation), equipped with a LynxEye detector that efficiently removes the Mn fluorescence. The powders were spread on Si zero background discs. NIST Si was added as an internal standard to correct the 2θ-scale. Neutron powder diffraction (NPD) data were collected at the ISIS time-of-flight neutron source at the Rutherford-Appleton laboratory in the UK with the POLARIS diffractometer [21]. Samples were placed in 6 to 8 mm diameter V cans. Structure refinements by the Rietveld method were carried out with the FullProf program [22], using both PXRD and NPD data (further details in the Supporting Information (SI)). The elemental compositions of the LNM powders were determined by inductively coupled plasma optical emission spectrometry (ICP-MS) analysis, carried out on a Spectro Arcos spectrometer (Spectro Analytical Instruments). Nitrogen physisorption experiments were performed (Micromeritics Tristar 3000) to determine the surface area and porosity of the LNM powders using the Brunauer−Emmett−Teller (BET) theory, T-plot, and Barrett−Joyner−Halenda (BJH) theory. Prior to BET analysis the powder samples were degassed at 250 °C for 12 hours. The surface morphologies of the samples were observed for the powder samples mounted on conductive carbon tape, employing a field-emission scanning electron microscope (Zeiss GeminiSEM 450) equipped with a ThermoFisher EDX detector. Dynamic light scattering (DLS) measurements were performed on a Brookhaven ZetaPALS/90Plus, after dispersing the powders in Milli-Q water. X-ray photoelectron spectroscopy (XPS) measurements were performed with a Thermo Scientific

multilab-2000 spectrometer. The XPS spectra were analyzed using CasaXPS software (version 2.3.16). The binding energy of C 1s (284.6 eV) was employed for the calibration of the energy scale of all the spectra. Line syntheses of elemental spectra were conducted with Gaussian–Lorentzian (70:30) curve and fitted using linear background subtraction. The powders were prepared for transmission electron microscopy (TEM) analysis by lightly grinding a small amount of powder, ultrasonicating them in ethanol for 10 minutes and settling for 5 minutes. The mixture was then dispersed onto a holey carbon Cu grid. TEM data were acquired on an aberration-corrected Themis Z (Thermo Fischer, 300 kV, STEM mode). This instrument is equipped with a Quantum post-column energy filter (Gatan Inc.) capable of dual-EELS, as well as a high-efficiency Super-X EDX detector (Thermo Fischer). EDX maps were acquired by scanning with a probe current of 100 pA, a pixel size on the order of 1 nm, and a dwell time of 1.8 ms. The high-resolution STEM image was acquired with a probe current of 10 pA and a dwell time of 5 µs. The EELS map was recorded in dual-EELS mode with a probe current of 50 pA, a pixel dwell time of 1.8 ms, a convergence angle of 21.4 mrad, and a collection angle of 23 mrad. $^{7}$Li magic angle spinning nuclear magnetic resonance (MAS NMR) experiments were performed at a magnetic field strength of 14.1 T (233.23 MHz Larmor frequency) with a Bruker Avance-III NMR spectrometer equipped with a 1.3 mm MAS probe head. The 60.00 kHz MAS rate was employed. 1D acquisitions involved a rotor-synchronized, double-adiabatic spin-echo sequence with a 90° excitation pulse of 1.00 µs followed by a pair of 50.0 µs tanh/tan short, high-power adiabatic pulses (SHAPs) with 5 MHz frequency sweep[23,24]. All pulses operated at the nutation frequency of 250 kHz. 4096 signal transients with 0.5 s relaxation delay were collected. The 2D aMAT experiment [25] involved the same pulses and power levels as 1D acquisitions, and 512 scans with a 0.5 s relaxation delay collected for each $t_1$ point. The $^{7}$Li chemical shifts were referenced with respect to solid LiF.

The electrodes for electrochemical testing were prepared by mixing 85 wt% active material with 10 wt% conductive carbon Super-P (Alfa Aesar) and 5 wt% polyvinylidene fluoride (PVDF, Sigma-Aldrich) dissolved N-methyl pyrrolidinone (NMP) by ball milling (Retsch® MM400) for 45 min at 25 Hz with 8 balls (Zirconia balls of 0.7 cm diameter). The obtained slurry was coated on Al current collector using a laboratory doctor blade technique with a wet thickness of 150 µm and dried at 65 °C overnight. The dried foils were punched out to be circular electrodes (12 mm diameter) then roll-pressed and again dried under vacuum at 100 °C for 24 h before being transferred into an Ar-filled glovebox ($H_2O$ < 0.5 ppm). The active material loading was 3 mg cm$^{-2}$. The electrochemical performance of all the samples was tested in half cell coin cells (2032R). A lithium metal foil pressed into a stainless-steel current collector disc was used as the negative electrode and a microporous monolayer polypropylene membrane (Celgard 2400) was used as a

separator. The separator was soaked with electrolyte solution (1.2M $LiPF_6$ in ethylene carbonate (EC)/ethyl methyl carbonate (EMC)/dimethyl carbonate (DMC) + 2 wt% vinylene carbonate (VC) + 2 wt% fluoroethylene carbonate (FEC) (Solvionic)). After an overnight open circuit potential period, the cells underwent galvanostatic cycling in the potential window of 4.8 V and 2 V vs $Li^+/Li$ using a VMP3Z biologic multichannel potentiostat/galvanostat at room temperature. For the galvanostatic intermittent titration technique (GITT), the cells were subjected to constant current pulses of C/20 for 30 minutes followed by a relaxation time interval of 2 h.

**Results and discussion**

Table 1 presents the experimentally verified elemental composition (by means of ICP-MS) of the samples with nominal composition $Li_{1.1}Ni_{0.35}Mn_{0.55}O_2$ treated at 700, 800, and 900 °C, along with their specific surface area (as determined with nitrogen physisorption) and mean effective diameter (as determined with DLS). According to ICP-MS analysis, the experimentally determined element ratios of the samples were in good agreement with the theoretical ratios. With increasing calcination temperature, there is a notable decrease in specific area and increase in mean effective diameter. This may have a positive effect on the functional properties, as the size of cobalt-free lithium-rich layered oxide particles was previously shown to have a dramatic effect on their electrochemical performance[26]. Larger particles with less specific surface area which leads to less surface degradation and thus experience a lower extent of capacity fade.

**Table 1** ICP and nitrogen physisorption results for the LNM samples synthesized using spray pyrolysis. Errors for the ICP measurements and specific area are 0.01 and 1, respectively.

| Sample | Nominal composition | ICP (Li:Ni:Mn) | Specific surface area ($m^2 g^{-1}$) |
|---|---|---|---|
| **LNM7** | $Li_{1.1}Ni_{0.35}Mn_{0.55}O_2$ – 700 °C | 1.09:0.35:0.55 | 31 |
| **LNM8** | $Li_{1.1}Ni_{0.35}Mn_{0.55}O_2$ – 800 °C | 1.07:0.35:0.55 | 17 |
| **LNM9** | $Li_{1.1}Ni_{0.35}Mn_{0.55}O_2$ – 900 °C | 1.09:0.35:0.55 | 9 |

XPS measurements were performed to examine the oxidation states of manganese and nickel on the surface of the materials. Figure SI-1 shows the binding energy regions of Mn 2p and Ni 2p core-level spectra for all the LNM samples. The $2p_{3/2}$ peaks in both Mn and Ni spectra have a greater area than that

of $2p_{1/2}$ peaks because of the spin-orbit splitting behavior. The core-level spectrum for Mn 2p shows two distinct peaks at binding energies of 642.5 eV ($2p_{3/2}$) and 653.5 eV ($2p_{1/2}$), corresponding to $Mn^{4+}$[24]. The core-level spectrum of Ni 2p shows peaks at binding energies of 854.5 eV ($2p_{3/2}$) and 872.4 eV ($2p_{1/2}$), which could be attributed to $Ni^{2+}$. The two less dominant satellite peaks at 860.0 eV and 879.0 eV further confirm the existence of $Ni^{2+}$[28].The deconvolution of the Mn 2p and Ni 2p spectra also clearly confirms the presence of $Mn^{4+}$ and $Ni^{2+}$ species. Therefore, the XPS results confirms that the transition metal elements present on the surface of all the samples were shows same chemical valences, observing no significant difference between the three materials synthesized at different calcination temperatures.

The crystal structure of the LNM materials was investigated by powder X-ray diffraction (refinement details can be found in the SI). The monoclinic (M) ($C2/m$ space group) and rhombohedral (R) ($R\bar{3}m$ space group) phases have similar structure but differ in cation ordering; $Li^+$ and $Mn^{4+}$ honeycomb ordering in the transition metal layer of $Li_2MnO_3$ results in the appearance of superstructure peaks in the PXRD pattern [29,30]. From crystal structure refinement, LNM7 is best refined as purely R phase, whereas LNM8 and LNM9 contain both M and R crystal phases, as can be clearly observed in Figure SI-2. Refined unit cell parameters for the phases as a function of synthesis temperature and residual indices for the structural models are presented in Table SI-1 and Table SI-2, respectively.

Based on the higher quality of the neutron powder diffraction (NPD) data, these were used in the final structure refinements. The NPD data showed that LNM7 contained also ~2 wt% $Li_2CO_3$. The structural models considered 25 refinable parameters, including 9 atomic positions for the M phase and 1 atomic position for the R phase. One collective atomic displacement parameter was used to obtain as accurate estimates of other parameters as possible. For the samples calcined at 800 and 900 °C, Ni was allowed to enter the M structure at Li-2b and Mn-4g sites by the substitution mechanism $3Ni^{2+} \leftrightarrow 2Li^+ + Mn^{4+}$. The 4g sites were assumed to be occupied by only Mn and Ni after substitution and it was additionally assumed that Mn does not move into other sites. One refined parameter thus determines the amount of Ni in the M structure and the cation distribution. The differences in neutron scattering lengths for Li, Mn, Ni and O, -0.190, -0.373, 1.03 and $0.5803 \times 10^{-14}$ m, respectively, provide for a good determination of site occupancies [31]. The composition of the R phases cannot be determined directly from the diffraction data alone and were determined from the nominal total composition of the sample and the refined scale factors of M and R, although indications are obtained by refining average cross-sections on the 3a TM and 3b Li metal sites. Mn, Ni, and Li were placed initially on the 3a site and Li on the 3b site. Ni and Li were then allowed to transfer between the 3a and 3b sites by one refinable parameter. Figure 1 shows calculated and observed NPD patterns (147° bank), unit cell volumes $V_n$ of M and R, as a function of

temperature and normalized to be per $MO_2$ unit, particle size distribution histograms of DLS, and nitrogen adsorption curves. Refined data using 52 ° bank together with residual indices, unit cell parameters, refined atomic coordinates for the M and R phases, metal-O distances for M phases in the transition metal layer and Li layer, metal-O distances for R phases and bond-valence sums for O atoms are given in Figure SI-3 and Tables SI-3 to SI-10. Good agreement between the structural models and neutron data was obtained as indicated by reliability indices; $R_F$ varies between 4 and 6% for the M phases, and between 2 and 5% for the R phases. Derived compositions for the phases at LNM7, LNM8, and LNM9 are given in Table 2, respectively, and corresponding derived distributions of cations are given in Tables 3 and 4. Errors from the refinements for the compositions and distributions are considerably less than corresponding to 1 at% and are here not given so as to not be misleading. They are included in corresponding Tables in the SI. The real errors are believed to correspond to a few at%.

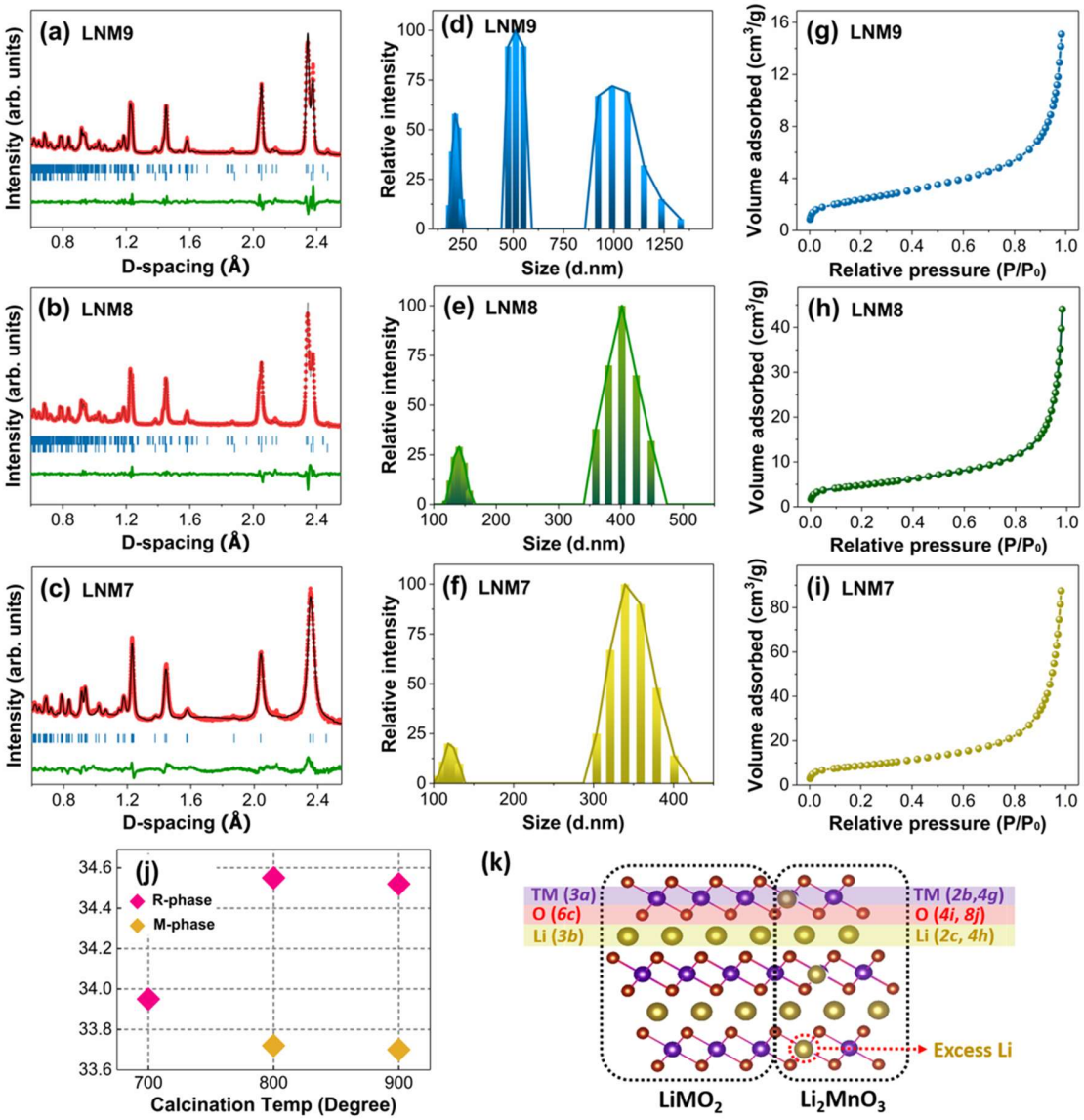


**Figure 1** Rietveld refinement using NPD patterns for (a) LNM9, (b) LNM8, (c) LNM7 samples (147° bank), showing their experimental data points (red), calculated patterns (black), their differences (blue), and Bragg diffraction positions (green sticks). The weak reflection at d = 2.14 Å is from V metal.; (d-f) Particle size distribution histograms of dynamic light scattering for (d) LNM9, (e) LNM8, (f) LNM7 samples; (g-i) Nitrogen adsorption curves of (g) LNM9, (h) LNM8, (i) LNM7 samples; (j) normalized unit cell parameters from NPD data for the R and M phases as a function of calcination temperature; (k) Schematic diagram of LNM crystal structure; the yellow, purple, and red balls represent lithium, transition metal, and oxygen, respectively.

**Table 2** Compositions of R and M phases derived from NPD data. Compositional errors are 0.01.

| | R-phase | | | | | M-phase | | | | |
|---|---|---|---|---|---|---|---|---|---|---|
| **Sample** | **Composition** | **%Li** | **%Ni** | **%Mn** | **Wt-%** | **Composition** | **%Li** | **%Ni** | **%Mn** | **Wt-%** |
| LNM7 | $Li_{1.1}Ni_{0.35}Mn_{0.55}O_2$ | 55 | 18 | 28 | 100 | - | - | - | - | - |
| LNM8 | $Li_{0.89}Ni_{0.67}Mn_{0.44}O_2$ | 44 | 33 | 22 | 43 | $Li_{1.23}Ni_{0.15}Mn_{0.62}O_2$ | 61 | 8 | 31 | 57 |
| LNM9 | $Li_{0.88}Ni_{0.68}Mn_{0.44}O_2$ | 44 | 33 | 22 | 45 | $Li_{1.245}Ni_{0.13}Mn_{0.62}O_2$ | 63 | 6 | 31 | 55 |

**Table 3** Cation distribution on 4g and 2b sites in M phases derived from NPD data.

| **Sample** | **composition 4g** | **% Ni** | **% Mn** | **composition 2b** | **% Li** | **% Ni** |
|---|---|---|---|---|---|---|
| LNM8 | $Ni_{0.30}Mn_{3.70}$ | 8 | 92 | $Li_{1.39}Ni_{0.61}$ | 70 | 30 |
| LNM9 | $Ni_{0.27}Mn_{3.73}$ | 7 | 93 | $Li_{1.47}Ni_{0.53}$ | 73 | 27 |

**Table 4** Cation distribution on 3a and 3b sites in R phases derived from NPD data.

| **Sample** | **composition 3a** | **% Li** | **% Ni** | **% Mn** | **composition 3b** | **% Li** | **% Ni** |
|---|---|---|---|---|---|---|---|
| LNM7 | $Li_{0.19}Ni_{0.27}Mn_{0.55}$ | 18 | 27 | 55 | $Li_{0.92}Ni_{0.08}$ | 92 | 8 |
| LNM8 | $Li_{0.078}Ni_{0.44}Mn_{0.48}$ | 8 | 44 | 48 | $Li_{0.81}Ni_{0.19}$ | 81 | 19 |
| LNM9 | $Li_{0.07}Ni_{0.49}Mn_{0.44}$ | 7 | 49 | 44 | $Li_{0.81}Ni_{0.19}$ | 81 | 19 |

Single phase LNM7 has Ni and Li disorder between the 3a and 3b sites, resulting in $[Li_{0.92}Ni_{0.08}]_{3b}[Li_{0.18}Ni_{0.27}Mn_{0.55}]_{3a}O_2$ as final refined formula. Refinements for the LNM8 and LNM9 reveals a composite structure of two crystal phases with M phase fraction in the range of 55-57% and no changes in their unit cell volumes. LNM9 contains a significant amount of Ni located in the 2b position (27%) of the M structure as well as Ni on the 3b site (19%) and Li on the 3a site (7%) of the R structure. Its formula as derived from NPD Rietveld refinement can be expressed in complex notation as $0.45(Li_{0.88}Mn_{0.44}Ni_{0.68}O_2) \cdot 0.55(Li_{1.87}Mn_{0.93}Ni_{0.20}O_3)$. The phase mixture is highly disordered compared to the ideal $R\bar{3}m$ and $C2/m$ crystal structures, as was previously reported for other layered materials in the form of cation mixing or antisite defect formation [32–34].

The $^{7}$Li MAS NMR spectra of LNM7, LNM8 and LNM9 are presented in Figure 2a. The spectra are broad as a result of anisotropic NMR interactions with unpaired electrons of paramagnetic centers and span nearly 4000 ppm. The extent of these paramagnetic interactions is similar for all samples, as the overall widths of the spectra and the number of discernible spinning sidebands do not change. Therefore, it can be assumed that the local lithium environments are similar in all three samples. With increasing calcination temperature, progressive narrowing of the individual sidebands is observed. Although for the studied systems the M and R phases cannot be distinguished in the 7Li NMR spectrum due to extensive paramagnetic broadening of the signals, the sharpening of the NMR resonances from the LMN7, LMN8, and LMN9 samples is in agreement with the NPD patterns in Fig. 1a, b, c, that reveal similar effect. This could be attributed to the occupational disorder and defects formation. The sharp signal at around 0 ppm in the spectrum of the LNM7 sample originates from a diamagnetic impurity (most probably $Li_2CO_3$ as detected by NPD pattern). This signal is significantly reduced in the spectrum of the LNM8 sample, and almost non-existent in the LNM9 sample. To provide additional structural insight, the two-dimensional aMAT spectrum was acquired (Figure 2b). In the projection along the F1 "isotropic" dimension of such a 2D spectrum, the effects of anisotropic paramagnetic NMR interactions are suppressed, revealing the isotropic NMR shifts. Two signals are observed at 720 ppm and at 1460 ppm. The first one accounts for the majority of signal intensity originating from lithium atoms accommodated in the Li layers, whereas the latter originate from the lithium atoms located in the transition metal layers. Although it evidences the Li/Ni exchange to some extent, the overall amount of Li in TM layers is small. These results agree well with the previously reported NMR data on similar systems [35,36].

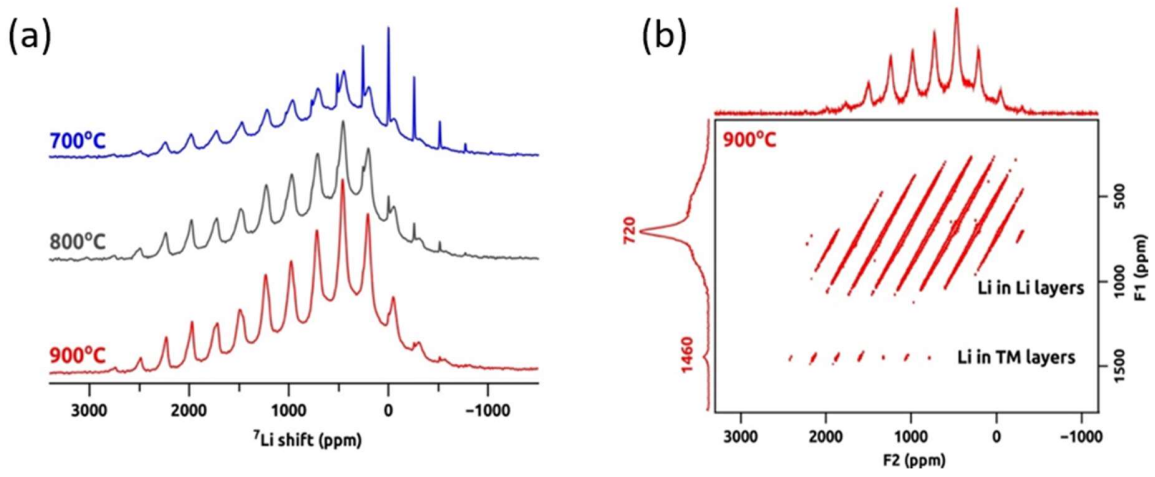


**Figure 2** a) 7Li MAS NMR spectra of the LNM7, LNM8 and LNM9 powder samples, b) Two-dimensional aMAT spectrum of the LNM9 powder sample.

The local structure and composition of LNM7, LNM8, and LNM9 were studied using aberration-corrected scanning transmission electron microscopy (STEM) combined with EDX and EELS (Figure 3). A representative overview of the particle morphology of LNM7, LNM8 and LNM9 show that the particle sizes increase with calcination temperature (Figure 3(a, d and g)), in agreement with DLS results presented in Table 1. The nanoparticle facets are also more pronounced in LNM8 and LNM9 powders. The corresponding elemental composition maps reveal that there is a strong chemical segregation in LNM9, where larger areas of Ni-enrichment are correlated to a drop in the Mn concentration. The Ni/Mn ratio closely follows morphological features, including Mn-rich regions as well as Ni-rich regions at the surfaces (Figure 3i).

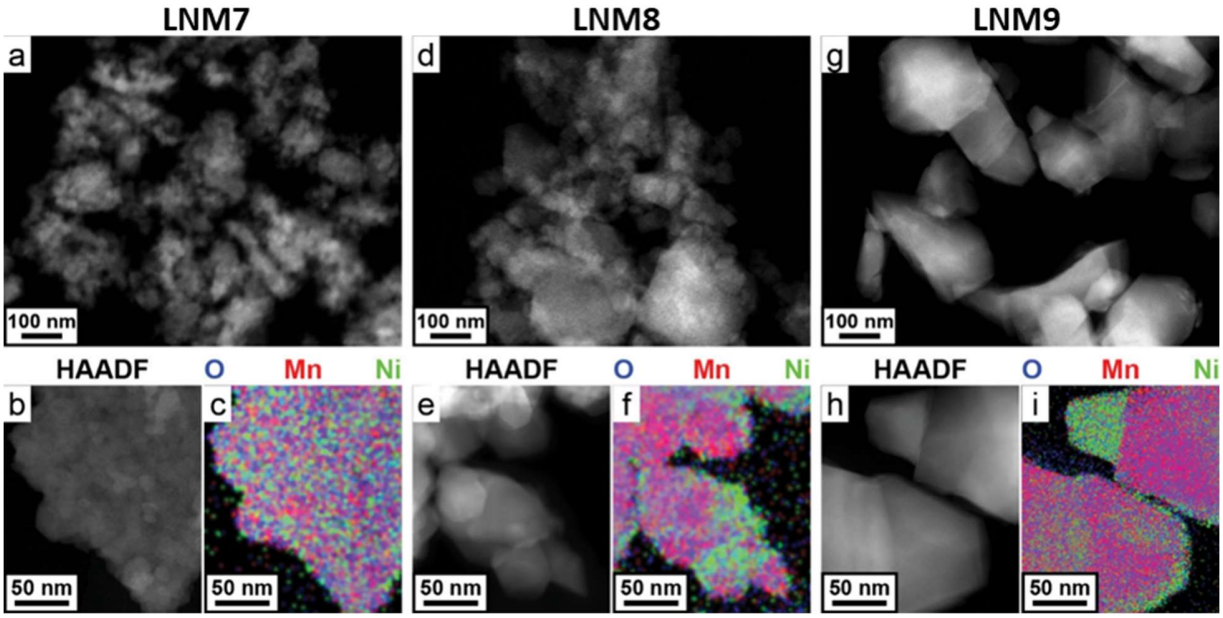


**Figure 3** HAADF overview of nanoparticle distribution from LNM7 (a), LNM8 (d), and LNM9 (g). Below, for each sample, a separate region was scanned for EDX, and the HAADF micrograph of this scanning region is presented along with a color composite image of the weight percentage of O (blue), Mn (red), and Ni (green). The HAADF overview and EDX maps were resampled to the same scale to emphasize differences in nanoparticle size and morphology.

To verify whether the compositional differences observed in LNM9 correspond to different structural phases, the particle pair shown in Figure 4 was investigated in further detail. Figure 4a presents a Z-contrast close-up of this region. The particle on the right indexes to the M-phase, with a series of stacking faults visible even with this relatively large field of view, and these are enlarged in the inset. This is a

common structural defect in $Li_2MnO_3$-related phases [30,37,38]. These stacking faults are most easily investigated by inspecting the Fourier Transform (FT) of this image (Figure 4b. A horizontal streak at the top captures the family of spots corresponding to the 020, 110, and $\bar{1}11$ reflections arising from the [1 0 0], $[1\bar{1}0]$, and [1 1 0] zone axes in the monoclinic phase, respectively. The real-space distribution of these orientations can be visualized by masking the corresponding reflections and inverting the FT back to real space. They are localized in the right-most particle and manifest themselves as vertical streaks. The respective inverse FT images were mapped to red, green, and blue color channels and the resulting false-color composite image is presented in Figure 4c. We observe a slight preference for the $[1\bar{1}0]$ orientation in this particle, noting that the thicker region to the right appears to almost exclusively favor this orientation. In addition to the stacking faults, the FT in Figure 4b shows a slight peak splitting on the reflection located in the yellow box and the inset enlargement. These two reflections correspond to the M-phase 001 and R-phase 003 reflections. An inverse FT of each of these individual reflections was calculated and the false-color composite image is displayed in Figure 4d. A clear separation of the R-phase and M-phase particles is observed, with the stacking faults exclusive to the M-phase. Interestingly, the fracture boundary separating these two particles does not appear to be the phase boundary, with the M-phase extending beyond this boundary into the R-phase particle as seen from Mn/Ni maps.

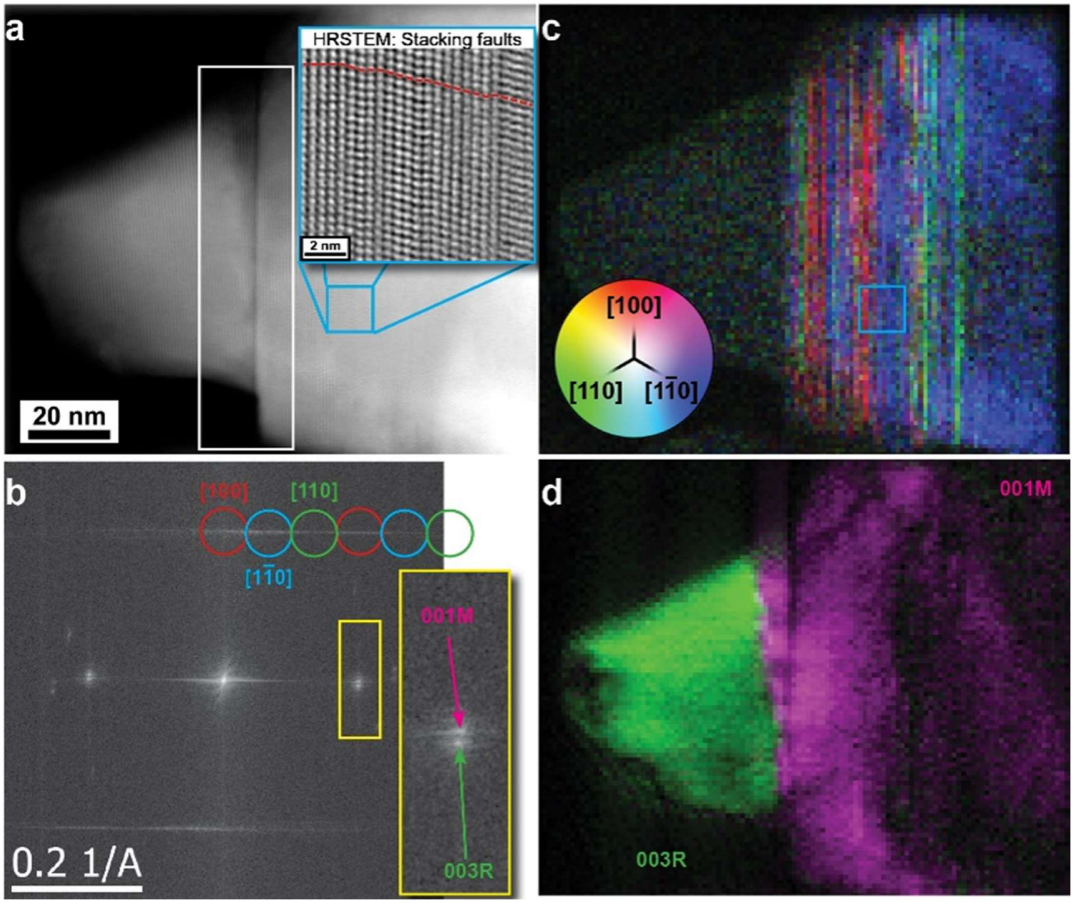


**Figure 4** (a) HAADF STEM image with a wide field-of-view. A close-up of stacking faults from this image is inset. The zone axis orientation of the two observed crystals is denoted. (b) FT of (a). The area within the yellow box is enlarged to show the peak splitting attributed to the 003R and 001M reflections. (c) Color composite image depicting the localization of stacking faults caused by local orientation of the M-phase. The FT masks used to generate the individual maps are presented with the corresponding color in (b). (d) A red/green map denoting the localization of the 001M (red) and 003R (green) reflections is shown in the yellow box.

The local chemistry of these two particles and their fracture/phase boundary was probed with simultaneously acquired EELS and EDX. Figure 5 presents a HAADF survey image of the LNM9 particle pair used to acquire low-loss EELS, core-loss EELS, and EDX, permitting a quantitative estimation of the local composition. Two boxes (1 and 2) are presented, denoting the region from which the raw EELS and EDX data were integrated for the spectra presented at right. Boxes 1 and 2 were deliberately placed to

investigate chemical differences between the monoclinic and rhombohedral structures. The core-loss EELS data from boxes 1 and 2 are shown in Figure 5b and c, respectively, along with the inelastic scattering cross-section (XS) models for the O-*K*, Mn-$L_{2,3}$, and Ni-$L_{2,3}$ edges used to quantify the composition. A clear increase in the Ni XS (determined by integrating over the by the solid green area after background subtraction) is observed in box 2 compared to box 1, while the ELNES (energy loss near edge structure) features on each of these edges show no discernible difference between the different phases, suggesting that the local cation valence states for both phases are similar. In Figure 5d, the corresponding low-loss EELS spectrum is displayed in the energy range from 40 – 90 eV, emphasizing the Mn-$M_{2,3}$, Li-*K*, and Ni-$M_{2,3}$ transitions. These spectra have been deconvoluted, stripped from their pre-edge backgrounds, and normalized to the post-edge region to emphasize differences in their respective inelastic scattering cross sections. We observe that the spectrum from box 1 (corresponding to the monoclinic phase) not only shows an increase in the Mn concentration but also the presence of an additional peak at approximately 61 eV loss, highlighted by the magenta arrow. This peak has been shown to be related to the Li-K edge in battery materials and we interpret its prominence in box 1 to reflect the higher Li concentration in the M-phase [39, 40]. In contrast, the Ni-$M_{2,3}$ edge is considerably more prominent in the spectrum from the R-phase. Figure 5e presents the integrated EDX data from the boxed regions 1 and 2. As with the core-loss EELS results, a clear increase in the Mn:Ni ratio in the monoclinic phase is observed. Table 5 summarizes the measured, calculated and refined compositions for the two phases in LNM9 from EELS, EDX, and NPD results. An excellent agreement is obtained between techniques confirming chemical compositions for the two crystal phases in LNM9. The Mn-rich regions show higher Li concentration and stacking faults, which are correlated to the monoclinic phase by inverse FT calculations. Highly segregated Ni-rich areas at the particles surface correspond to the R phase. These findings are consistent with the results from NPD.

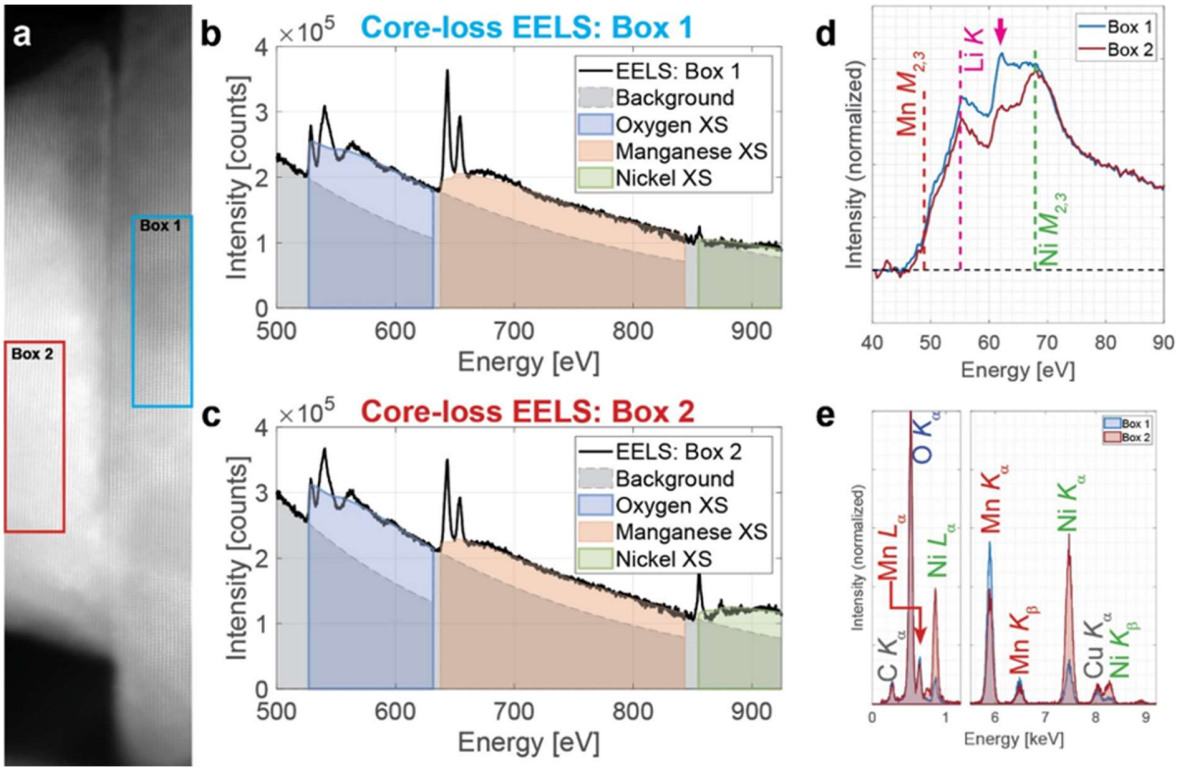


**Figure 5** (a) HAADF overview of the EELS / EDX scan region. Boxes corresponding to the summation regions from the monoclinic (Box 1) and rhombohedral (Box 2) phases are annotated. The summed spectra from these boxes are presented in (b) and (c), respectively. These also include the inelastic scattering cross-section models used for quantification. The models are convolved with the simultaneously acquired low-loss EELS spectrum to account for plural scattering. These spectra have been deconvolved, stripped from the pre-edge background, and normalized to the post-edge region for comparison purposes, (d) Mn, Ni, and Li edges from the low-loss EELS spectrum corresponding to the boxes in (a), (e) Simultaneously acquired EDX spectra from the boxes in (a). The spectra are normalized to the maximum intensity of the O-Kα peak.

**Table 5** Measured, calculated and refined stoichiometry from EELS, EDX, and NPD results for LNMO9. The relative error for EELS and EDX results is less than 5%, while it is less than 1% for NPD. For EDX, neither the Li nor the O edges are reliably detected. Therefore, we fixed the O composition at its nominal value and only measured the Ni:Mn ratio. The Li concentration (*in italics*) is calculated under the additional assumption of charge balance.

| | **EELS** | | **EDX** | | **NPD** | |
|---|---|---|---|---|---|---|
| **Elements** | Box 1 *(M-phase)* | Box2 *(R-phase)* | Box 1 *(M-phase)* | Box2 *(R-phase)* | *(M-phase)* | *(R-phase)* |
| Li | *1.3* | *0.8* | *1.2* | *0.9* | *1.24* | *0.88* |
| Ni | 0.2 | 0.7 | 0.2 | 0.7 | 0.13 | 0.68 |
| Mn | 0.5 | 0.5 | 0.6 | 0.4 | 0.62 | 0.44 |
| O | 2.0 | 2.0 | 2 | 2 | 2 | 2 |

Prior to electrochemical testing, the electrode homogeneity, i.e. uniformity of active material, carbon black and binder distribution, was assessed [41]. The cross-sectional SEM images and EDX Mn elemental maps for the three electrodes are presented in Figure SI-4. Electrodes with a mass loading of 3 mg $cm^{-2}$ contain agglomerates of more than 10 µm in size, which are randomly distributed between smaller agglomerates with sizes ranging from less than 1 µm up to a few µm. The EDX mapping shows a homogeneous Ni, Mn and O distribution, irrespective of the employed active material, and this ensures representative electrochemical results as a function of active material calcination temperature rather than artifact effects related to electrode processing.

The electrochemical characteristics of LNM7, LNM8, and LNM9 electrodes were evaluated by galvanostatic cycling in half cell configuration, within the potential window of 4.8 to 2 V vs. $Li^+/Li$. Figure 6(a-c) shows the galvanostatic charge/discharge profiles of the three electrodes, and the corresponding differential capacity profiles (dQ/dV) are plotted in Figure 6(d-f). The initial three charge-discharges were performed at C/20 rate to stabilize the cathode-electrolyte interface (CEI). Thereafter, the cells were cycled at C/3. During activation, all cells exhibit a slanted potential curve during first charging below 4.5 V vs $Li^+/Li$, which is attributed to the oxidation of $Ni^{2+}$ to $Ni^{4+}$. The subsequent potential plateau at 4.5 V vs

$Li^+/Li$ is assigned to the removal of lithium ions and oxygen loss from the monoclinic phase[13]. Further cycling results in a phase transformation, which can be monitored using dQ/dV plots (Figure 6d). In the $1^{st}$ and $2^{nd}$ cycle, the peaks at 3.75 V vs $Li^+/Li$ (charging) and at 3.6 V vs $Li^+/Li$ (discharging) correspond to redox activity of nickel, whereas the peak at 4.55 V vs $Li^+/Li$ (charging) corresponds to irreversible oxygen loss. The redox process at 3.3 V vs $Li^+/Li$ (discharging) corresponds to the reduction of $Mn^{4+}$, together with the $Li^+$ insertion into the monoclinic phase[42]. These peaks vanish with prolonged cycling (e.g. after 50 and 150 cycles), and a broad cathodic peak related to the $Mn^{4+}/Mn^{3+}$ redox process appears in the voltage range of 2.7-3.2 V vs $Li^+/Li$. This is the characteristic voltage range of $Mn^{4+}$ reduction in Mn-based spinel cathodes materials [43,44]. For LNM9, the voltage decay associated with $Mn^{4+}/Mn^{3+}$ redox activity is 0.5 V after 100 cycles, in accordance with the severe layered-to-spinel-type phase transformation occurring in the material during charge-discharge [42]. This is not the case for LNM7, which exhibits no redox peaks observed for cycles 50 and 150 (figure 6f). The Comparative cycling performance of the LNM9, LNM8 and LNM7 are shown in figure 6g. LNM9 initially exhibits a discharge capacity of 160 mAh/g at C/3, with a capacity retention of 80% after 150 cycles. LNM8 has a discharge capacity of 120 mAh/g at C/3 with the capacity retention of 69% after 150 cycles. In contrast, LNM7 delivers no significant discharge capacity after 50 cycles. The extent of voltage decay of these cathodes were represented by plotting the average discharge voltage vs. cycle number (figure SI-5). Both LNM9 and LNM8 cathodes exhibit relatively slow average discharge voltage decay. Whereas, LNM7 cathode exhibits abrupt voltage decay as cycling progresses. Further the rate capability of the LNM cathodes were assessed through galvanostatic charge/discharge tests at several rates and the obtained discharge capacities are shown in Figure 6h. The LNM9 cathode shows relatively high and stable capacities of 200, 180, 135, 100, and 135 mAh/g at current rates of C/20, C/10, C/3, 1C, C/3, respectively, whereas these values are 160, 135, 100, 35, and 100 mAh/g for the LNM8 electrode. The highly segregated structure of the LNM9 particles outperforms both LNM8 and single-phase LNM7.

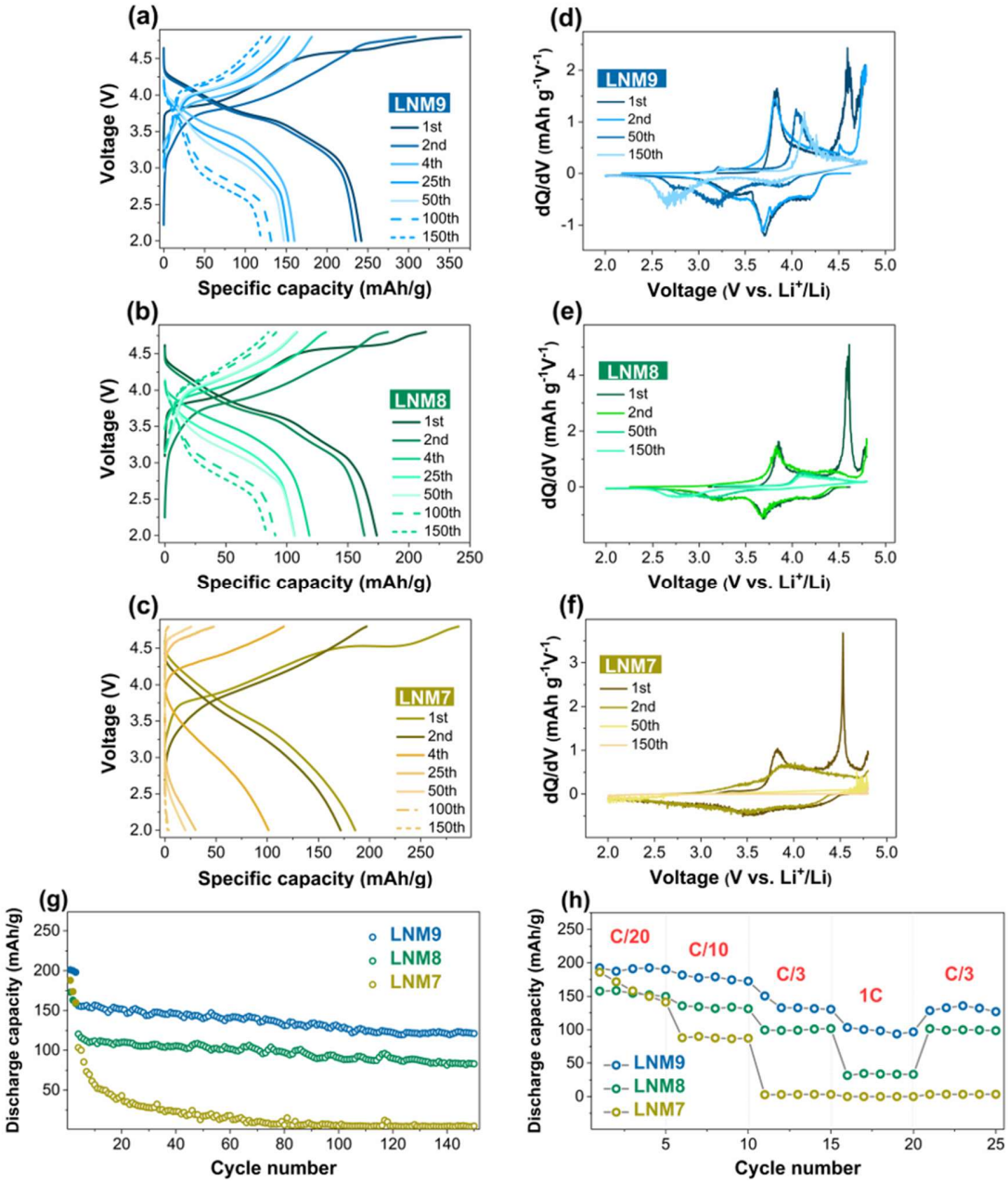


**Figure 6** Galvanostatic charge/discharge curves of the LNM9, LNM8, and LNM7 electrodes (a-c), and their corresponding differential capacity profiles dQ/dV (d-f). The initial three charge-discharges were carried at C/20 rate to stabilize the cathode-electrolyte interface (CEI), after that the cells were cycled at C/3 rate. (g) Comparative cycling performance of the LNM7, LNM8, and LNM9 electrodes. The initial three charge-discharge cycles were performed at C/20 rate followed by cycling at C/3 rate. (h) C-rate capability of the LNM7, LNM8, and LNM9 electrodes.

Electrochemical impedance spectroscopy (EIS) has been employed to elucidate the improved performance of the LNM9 electrode. Figure 7(a, b) displays the Nyquist plots for fresh cells and cycled cells. As shown the Nyquist plots show the charge-transfer semicircle and a slope at low frequency attributed to lithium ion diffusion in the bulk material. The intercept in high frequency represents the solution resistance ($R_s$) and values are almost the same for all the samples, indicating the ohmic polarizations of the investigated samples can be neglected. The charge-transfer resistance ($R_{ct}$) value of fresh electrodes are 160 Ω, 210 Ω and 340 Ω for LNM9, LNM8 and LNM7 cathodes respectively. Upon cycling, the charge-transfer resistance ($R_{ct}$) value of cathode LNM9 (205 Ω) is much smaller than that of the LNM8 cathode (565 Ω). The lower charge-transfer resistance of the LNM9 electrode after 150 cycles reflects an improved quality of the cathode interface and faster electronic conductivity. This is agreement with the electrochemical performance of LNM9 cathode as presented in figure 6.

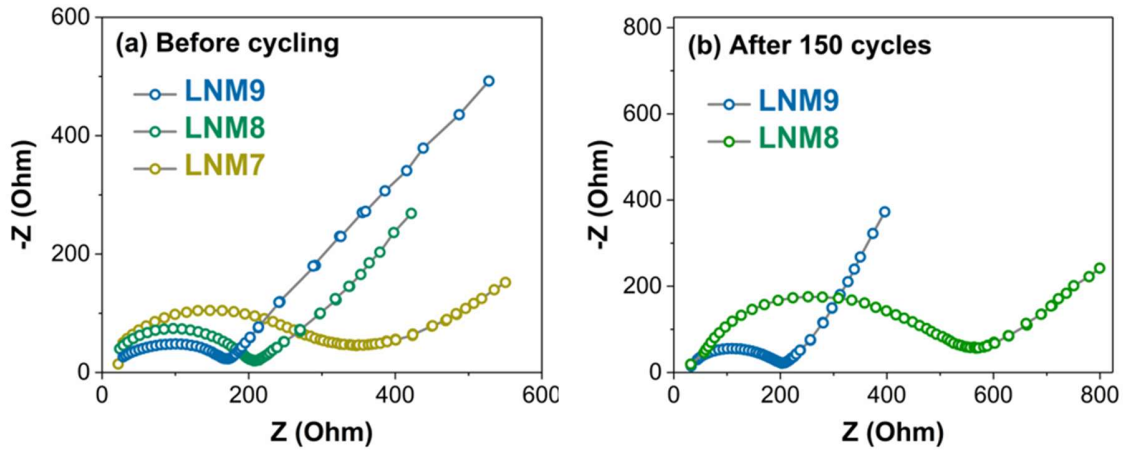


**Figure 7** Nyquist plots of LNM7, LNM8, and LNM9 electrodes (a) before cycling and (b) after 150 cycles.

GITT measurement was conducted to evaluate the chemical diffusion coefficient of lithium ions ($D_{Li^+}$) in the LNM9 electrode (Figure SI-6a). The initial charge step to 4.4 V vs $Li^+/Li$ is associated with lithium ion deintercalation from the R phase exhibits a maximum Li-ion diffusion coefficient value of $10^{-10}$ $cm^2$ $s^{-1}$ and further charging from 4.4 V corresponds to $D_{Li+}$ values associated with the kinetically controlled activation process of the M phase, which decreases abruptly to $D_{Li+}$ value of $10^{-14}$ $cm^2$ $s^{-1}$. During the subsequent discharge processes from 4.8 to 2.0 V vs $Li^+/Li$, the LNM9 exhibits the same variation trends of the Li-ion diffusion coefficient of values which is around $10^{-10}$ $cm^2$ $s^{-1}$. The LNM9 exhibits a considerably good

diffusion coefficient in comparison with typical lithium rich layered cathode material such as $Li_{1.2}Ni_{0.13}Co_{0.13}Mn_{0.54}O_2$ ($10^{-10}$ $cm^2s^{-1}$ to $10^{-13}$ $cm^2$ $s^{-1}$)[45].

**Conclusions**

In this work, we demonstrated that a spray-pyrolysis synthesis method combined with controlled calcination paves a compelling new pathway to tune the structural properties and electrochemical performance of Co-free Li-rich layered oxides. Advanced powder neutron diffraction and STEM investigations show that $Li_{1.1}Ni_{0.35}Mn_{0.55}O_2$ material calcined at 900°C has a large particle size compared to samples calcined at lower temperatures, and a strong structural segregation of layered $R\bar{3}m$ (R) and $C2/m$ (M) phases in the particle, corresponding to Ni-rich facets on the outmost surfaces and Mn-rich regions, respectively. These effects can enhance the overall electrochemical performance. The $Li_{1.1}Ni_{0.35}Mn_{0.55}O_2$ cathode calcined at 900°C contains significant amounts of Ni located on the 4g position (7%) of the M structure as well as Ni on the 3b site (19%) and Li on the 3a site (7%) of the R structure. Its refined formula in complex notation is $0.45(Li_{0.88}Ni_{0.68}Mn_{0.44}O_2)\cdot 0.55(Li_{1.87}Ni_{0.20}Mn_{0.93}O_3)$. HAADF-STEM observations combined with EDX and EELS studies on the local structure and composition demonstrate that the refined crystal structure corresponds to segregated phases at the particle level, following morphological features as evidenced by the Ni-facets indexed as for the R phase. The material calcined at the highest temperature shows improved cycling performance (80% capacity retention after 150 cycles at C/3), high rate capability (100 mAh/g at 1C) and relatively slow average discharge voltage decay as compared to the materials calcined at lower temperature. The formation of larger, structurally segregated particles alleviates cathode degradation, improving the electrochemical performance in various aspects, such as specific capacity, rate capability, and electrochemical stability. This work provides a simple but effective strategy to improve the performance of Li-rich layered oxides containing no cobalt for next-generation Li-ion batteries.

**Supporting Information**

Structure refinements using PXRD data, Structure refinements using neutron data, Refined unit cell parameters for the phases, Residual indices for the structural models Cross-sectional SEM images acquired from the LNM cathodes, Average discharge voltage vs. cycle number plot for LNM cathodes and GITT measurements for LNM9 cathode.

**Acknowledgements and Funding**

The authors acknowledge funding from Generalitat de Catalunya 2017 SGR 1246 and 2017 SGR 327 and the Spanish MINECO project ENE2017-85087-C3. IREC is funded by the CERCA Programme/Generalitat de Catalunya. IREC also acknowledges additional support from the European Regional Development Funds (ERDF, FEDER). This research was funded by HORIZON 2020-supported EU project COBRA, grant number H2020-EU.3.4.-875568. The authors also acknowledge Stephen hull and Ron smith for collecting neutron data at the ISIS neutron and muon source using rapid access. The experiment number was 2000189.

**REFERENCES**

1. Etacheri, V., Marom, R., Elazari, R., Salitra, G., and Aurbach, D. (2011) Challenges in the development of advanced Li-ion batteries: A review. *Energy Environ. Sci.*, **4** (9), 3243–3262.

2. Tidblad, A.A., Edström, K., Hernández, G., de Meatza, I., Landa-Medrano, I., Jacas Biendicho, J., Trilla, L., Buysse, M., Ierides, M., Horno, B.P., Kotak, Y., Schweiger, H.-G., Koch, D., and Kotak, B.S. (2021) Future Material Developments for Electric Vehicle Battery Cells Answering Growing Demands from an End-User Perspective. *Energies*, **14** (14), 4223.

3. Booth, S.G., Nedoma, A.J., Anthonisamy, N.N., Baker, P.J., Boston, R., Bronstein, H., Clarke, S.J., Cussen, E.J., Daramalla, V., De Volder, M., Dutton, S.E., Falkowski, V., Fleck, N.A., Geddes, H.S., Gollapally, N., Goodwin, A.L., Griffin, J.M., Haworth, A.R., Hayward, M.A., Hull, S., Inkson, B.J., Johnston, B.J., Lu, Z., MacManus-Driscoll, J.L., Martínez De Irujo Labalde, X., McClelland, I., McCombie, K., Murdock, B., Nayak, D., Park, S., Pérez, G.E., Pickard, C.J., Piper, L.F.J., Playford, H.Y., Price, S., Scanlon, D.O., Stallard, J.C., Tapia-Ruiz, N., West, A.R., Wheatcroft, L., Wilson, M., Zhang, L., Zhi, X., Zhu, B., and Cussen, S.A. (2021) Perspectives for next generation lithium-ion battery cathode materials. *APL Mater.*, **9** (10), 109201.

4. Wang, X., Ding, Y.L., Deng, Y.P., and Chen, Z. (2020) Ni-Rich/Co-Poor Layered Cathode for Automotive Li-Ion Batteries: Promises and Challenges. *Adv. Energy Mater.*, **10** (12), 1–28.

5. Thackeray, M.M., Kang, S.H., Johnson, C.S., Vaughey, J.T., Benedek, R., and Hackney, S.A. (2007) Li2MnO3-stabilized LiMO2 (M = Mn, Ni, Co) electrodes for lithium-ion batteries. *J. Mater. Chem.*, **17** (30), 3112–3125.

6. Johnson, C.S., Korte, S.D., Vaughey, J.T., Thackeray, M.M., Bofinger, T.E., Shao-Horn, Y., and Hackney, S.A. (1999) Structural and electrochemical analysis of layered compounds from Li2MnO3. *J. Power Sources*, **81**–**82**, 491–495.

7. Assat, G., and Tarascon, J.M. (2018) Fundamental understanding and practical challenges of anionic redox activity in Li-ion batteries. *Nat. Energy*, **3** (5), 373–386.

8. Kim, D., Croy, J.R., and Thackeray, M.M. (2013) Comments on stabilizing layered manganese oxide electrodes for Li batteries. *Electrochem. commun.*, **36**, 103–106.

9. Armstrong, A.R., Holzapfel, M., Novák, P., Johnson, C.S., Kang, S.H., Thackeray, M.M., and Bruce, P.G. (2006) Demonstrating oxygen loss and associated structural reorganization in the lithium battery cathode Li[Ni0.2Li0.2Mn 0.6]O2. *J. Am. Chem. Soc.*, **128** (26), 8694–8698.

10. Thackeray, M.M., Kang, S.H., Johnson, C.S., Vaughey, J.T., and Hackney, S.A. (2006) Comments on the structural complexity of lithium-rich Li1+xM1-xO2 electrodes (M = Mn, Ni, Co) for lithium batteries. *Electrochem. commun.*, **8** (9), 1531–1538.

11. Mohanty, D., Li, J., Abraham, D.P., Huq, A., Payzant, E.A., Wood, D.L., and Daniel, C. (2014) Unraveling the voltage-fade mechanism in high-energy-density lithium-ion batteries: Origin of the tetrahedral cations for spinel conversion. *Chem. Mater.*, **26** (21), 6272–6280.

12. Mohanty, D., Kalnaus, S., Meisner, R.A., Safat, A.S., Li, J., Payzant, E.A., Rhodes, K., Wood, D.L., and Daniel, C. (2013) Structural transformation in a Li1.2Co0.1Mn 0.55Ni0.15O2 lithium-ion battery cathode during high-voltage hold. *RSC Adv.*, **3** (20), 7479–7485.

13. Hu, S., Pillai, A.S., Liang, G., Pang, W.K., Wang, H., Li, Q., and Guo, Z. (2019) *Li-Rich Layered Oxides and Their Practical Challenges: Recent Progress and Perspectives*, Electrochemical Energy Reviews 2019, 1-35.

14. Prakasha, K.R., Sathish, M., Bera, P., and Prakash, A.S. (2017) Mitigating the Surface Degradation and Voltage Decay of Li1.2Ni0.13Mn0.54Co0.13O2 Cathode Material through Surface Modification Using Li2ZrO3. *ACS Omega*, **2** (5), 2308–2316.

15. Prakasha, K.R., and Prakash, A.S. (2015) A time and energy conserving solution combustion synthesis of nano Li1.2Ni0.13Mn0.54Co0.13O2 cathode material and its performance in Li-ion batteries. *RSC Adv.*, **5** (114), 94411–94417.

16. Nie, L., Liang, C., Chen, S., He, Y., Liu, W., Zhao, H., Gao, T., Sun, Z., Hu, Q., Zhang, Y., Yu, Y., and Liu, W. (2021) Improved Electrochemical Performance of Li-Rich Layered Oxide Cathodes Enabled by a Two-Step Heat Treatment. *ACS Appl. Mater. Interfaces*, **13** (11), 13281–13288.

17. Alagar, S., Karuppiah, C., Madhuvilakku, R., Piraman, S., & Yang, C.-C. (2019) Temperature-Controlled Synthesis of Li- and Mn-Rich Li1.2Mn0.54Ni0.13Co0.13O2 Hollow Nano/Sub-Microsphere Electrodes for High-Performance Lithium-Ion Battery. ACS Omega. **4**, (23) 2019, 20285–20296.

18. Wang, D., Yu, R., Wang, X. (2015) Dependence of Structure and Temperature for Lithium-rich Layered-spinel Microspheres Cathode Material of Lithium Ion Batteries. Scientific Reports 5 8403 – 8410.

19. Y. Chen, S. Luo, J. Leng, S. Deng, S. Yan, X. Tian, Y. Li, J. Guo, T. Lei, J. Zheng, J. (2021) Exploring the synthesis conditions and formation mechanisms of Li rich layered oxides via solid-state method. Alloy. Compd. 854 157204.

20. Samuel O.Ajayi, Cyril O.Ehi-Eromosele, Kolawole O.Ajanaku. (2022) Combustion synthesis and characterization of Li1.2Mn0.52Ni0.20Co0.08O2 cathodes for Li-Ion battery: Effect of fuel mixture and annealing temperature. Ceramics International, 48, 2. 2306 - 2316.

21. Smith, R.I., Hull, S., Tucker, M.G., Playford, H.Y., McPhail, D.J., Waller, S.P., and Norberg, S.T. (2019) The upgraded Polaris powder diffractometer at the ISIS neutron source. *Rev. Sci. Instrum.*, **90** (11). 115101

22. Rodriguez-Carvajal. J. (1990) No Title. *FULLPROF A Progr. Rietveld Refinement Pattern Matching Anal.*, 127.

23. Hwang, T.L., Van Zijl, P.C.M., and Garwood, M. (1998) Fast Broadband Inversion by Adiabatic Pulses. *J. Magn. Reson.*, **133** (1), 200–203.

24. Kervern, G., Pintacuda, G., and Emsley, L. (2007) Fast adiabatic pulses for solid-state NMR of paramagnetic systems. *Chem. Phys. Lett.*, **435** (1–3), 157–162.

25. Clément, R.J., Pell, A.J., Middlemiss, D.S., Strobridge, F.C., Miller, J.K., Whittingham, M.S., Emsley, L., Grey, C.P., and Pintacuda, G. (2012) Spin-transfer pathways in paramagnetic lithium transition-metal phosphates from combined broadband isotropic solid-state MAS NMR spectroscopy and DFT

calculations. *J. Am. Chem. Soc.*, **134** (41), 17178–17185.

26. Li, J., Shunmugasundaram, R., Doig, R., and Dahn, J, R. (2016) In-situ X-ray Diffraction Study of Layered Li-Ni-Mn-Co Oxides: Effect of Particle Size and Structural Stability of Core-Shell MaterialsChem. Mater. **28** (1) 162–171.

27. Lim, J.; Moon, J.; Gim, J.; Kim, S.; Kim, K.; Song, J.; Kang, J.; Ima, W. B.; Kim, J. (2012) Fully activated Li2MnO3 nanoparticles by oxidation reaction. J. Mater. Chem., **22**, 11772–11777.

28. Meng, J.; Zhang, S.; Wei, X.; Yang, P.; Wang, S.; Wang, J.; Li, H.; Xing, Y.; Liu, G. (2015) Synthesis, Structure and Electrochemical Properties of Lithium-Rich Cathode Material Li1.2Mn0.6Ni0.2O2 Microspheres. RSC Adv. 5, 81565−81572.

29. Sears Boulineau, A., Croguennec, L., Delmas, C., and Weill, F. (2010) Structure of Li2MnO3 with different degrees of defects. *Solid State Ionics*, **180** (40), 1652–1659.

30. Matsunaga, T., Komatsu, H., Shimoda, K., Minato, T., Yonemura, M., Kamiyama, T., Kobayashi, S., Kato, T., Hirayama, T., Ikuhara, Y., Arai, H., Ukyo, Y., Uchimoto, Y., and Ogumi, Z. (2016) Dependence of Structural Defects in Li2MnO3 on Synthesis Temperature. *Chem. Mater.*, **28** (12), 4143–4150.

31. Sears, V. F. (1992) Neutron scattering lengths and cross sections. *Neutron News*, **3**(3), 26-37.

32. Orlova, E.D., Savina, A.A., Abakumov, S.A., Morozov, A. V., and Abakumov, M. (2021) SS symmetry Cathodes for Li-Ion Batteries. **2**, 1–15.

33. Yin, L., Li, Z., Mattei, G.S., Zheng, J., Zhao, W., Omenya, F., Fang, C., Li, W., Li, J., Xie, Q., Erickson, E.M., Zhang, J.G., Whittingham, M.S., Meng, Y.S., Manthiram, A., and Khalifah, P.G. (2020) Thermodynamics of Antisite Defects in Layered NMC Cathodes: Systematic Insights from High-Precision Powder Diffraction Analyses. *Chem. Mater.*, **32** (3), 1002–1010.

34. Jacas Biendicho, J., Hemesh, A., Izquierdo, V., Flox, C., and Morante, J.R. (2021) Contact resistance stability and cation mixing in a Vulcan-based LiNi1/3Co1/3Mn1/3O2slurry for semi-solid flow batteries. *Dalt. Trans.*, **50** (19), 6710–6717.

35. Bréger, J., Kang, K., Cabana, J., Ceder, G., and Grey, C.P. (2007) NMR, PDF and RMC study of the positive electrode material Li(Ni0.5Mn0.5)O2 synthesized by ion-exchange methods. *J. Mater. Chem.*, **17** (30), 3167–3174.

36. Cabana, J., Chernova, N.A., Xiao, J., Roppolo, M., Aldi, K.A., Whittingham, M.S., and Grey, C.P. (2013) Study of the Transition Metal Ordering in Layered Na. *Inorg. Chem.*, **52**, 8540–8550.

37 Shunmugasundaram, R., Arumugam, R.S., and Dahn, J.R. (2016) A Study of Stacking Faults and Superlattice Ordering in Some Li-Rich Layered Transition Metal Oxide Positive Electrode Materials. *J. Electrochem. Soc.*, **163** (7), A1394–A1400.

38. Reynaud, M., and Casas-Cabanas, M. (2017) Order and disorder in NMC layered materials: A FAULTS simulation analysis. *Powder Diffr.*, **32** (S1), S213–S220.

39. Muto, S.; Tatsumi, K. (2017) Detection of Local Chemical States of Lithium and Their Spatial Mapping by Scanning Transmission Electron Microscopy, Electron Energy-Loss Spectroscopy and Hyperspectral Image Analysis. Microscopy, **66** (1), 39–49.

40. Wang, F.; Graetz, J.; Moreno, M. S.; Ma, C.; Wu, L.; Volkov, V.; Zhu, Y. (2011) Chemical Distribution and Bonding of Lithium in Intercalated Graphite: Identification with Optimized Electron Energy Loss Spectroscopy. ACS Nano, **5** (2), 1190–1197.

41. Yari, S., Hamed, H., D'Haen, J., Van Bael, M.K., Renner, F.U., Hardy, A., and Safari, M. (2020) Constructive versus Destructive Heterogeneity in Porous Electrodes of Lithium-Ion Batteries. *ACS Appl. Energy Mater.*, **3** (12), 11820–11829.

42. Li, L., Song, B.H., Chang, Y.L., Xia, H., Yang, J.R., Lee, K.S., and Lu, L. (2015) Retarded phase transition by fluorine doping in Li-rich layered Li1.2Mn0.54Ni0.13Co0.13O2 cathode material. *J. Power Sources*, **283**, 162–170.

43. Zhao, C., Wang, X., Liu, R., Liu, X., and Shen, Q. (2014) Oxalate precursor preparation of Li1.2Ni0.13Co0.13Mn0.54O2 for lithium ion battery positive electrode. *Ionics (Kiel).*, **20** (5), 645–652.

44. Nayak, P.K., Grinblat, J., Levi, M., Levi, E., Kim, S., Choi, J.W., and Aurbach, D. (2016) Al Doping for Mitigating the Capacity Fading and Voltage Decay of Layered Li and Mn-Rich Cathodes for Li-Ion Batteries. *Adv. Energy Mater.*, **6** (8), 1–13.

45 Li, H., Wei, X., Yang, P., Ren, Y., Wang, S., Xing, Y., and Zhang, S. (2018) Uniform Li1.2Ni0.13Co0.13Mn0.54O2 hollow microspheres with improved electrochemical performance by a facile solvothermal method for lithium ion batteries. Electrochimica Acta, **261**, 86–95.

**TOC Graphic**

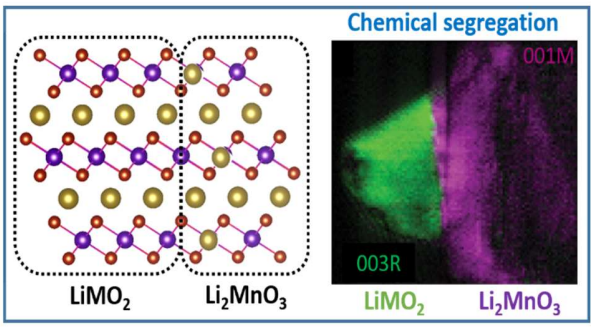
Chemical segregation
001M
003R
LiMO2
Li2MnO3
LiMO2
Li2MnO3